Optimization of Balanced Detector for Coherent Receiver on Generic InP Platform by Particle Swarm Optimization

Dhiman Nag, Weiming Yao, *Member, IEEE*, and Jos J. G. M. van der Tol

Abstract— **The balanced photodetector (BPD) is an important component for high-speed coherent receiver. An optimization strategy of waveguide-based multi-quantum well (MQW) BPDs, operating at 1550 nm is demonstrated on a generic InP platform. Design parameters of BPD are optimized towards achieving the highest bandwidth for a responsivity through an algorithm based on Particle Swarm Optimization (PSO). We do so by establishing an equivalent circuit model of BPD and analyzing its opto-electronic transfer function through numerical modelling. We address the major bottlenecks of high-speed BPDs: transit time of generated carriers and RC loading in our model. The algorithm is able to provide multiple combinations of design parameters with the same output characteristics. The design methodology to integrate laser with optimized BPD is presented to successfully implement a coherent receiver.**

Index Terms— **Photonic integrated circuits, high-speed coherent receiver, particle swarm optimization, MATLAB.**

I. INTRODUCTION

COHERENT balanced receivers are commonly used in high-speed photonic communication links operating at 1550 nm owing to their ability to suppress laser relative intensity noise (RIN) and to achieve high common mode rejection ratio (CMRR), high noise suppression etc. [1], [2], and [3]. They also enable the differential phase shift keying (DPSK) schemes due to balanced detection, which has nearly 3-dB more sensitivity compared to OOK [4], [5]. For successful implementation of balanced receivers, balanced detectors (BPDs) play a major role [6]. A BPD consists of two reverse-biased near-identical and near-isolated photodetectors (PDs) [6]. Separate optical inputs are fed to these PDs and their difference current is taken as the output. Different material platforms are investigated by many groups for realizing high-speed detectors at 1550 nm [7], [8], [9]. However, a generic integration platform is essential to embed several active and passive photonic building blocks (BBs) on the same chip that enables

a broad range of applications including telecommunication, sensing, quantum key distribution, imaging etc. [10]. This work is focused on optimization of the balanced detector (BPD) to be implemented in a coherent balanced receiver on a generic integration platform, based on InP/InGaAsP material system using monolithic butt-coupling technology [10], [11], [12]. The active components have quaternary InGaAsP core, tuned for emission or absorption. And, the passive components have a core of non-absorbing quaternary material. In order to exploit the benefits of a generic platform for coherent balanced receivers, BPD needs to be designed for optimum performance and monolithically integrated with laser, which works as the local oscillator. Multiple regrowth steps during butt-joint technology greatly increase the fabrication complexity and process time that leads to high cost and low yield. A MQW stack is used for the laser to enhance its emission efficiency [13]. We consider the same MQW stack for BPD to avoid additional regrowth. Two most essential figures of merit of detectors are its bandwidth and responsivity. They possess different and often opposite dependencies on certain dimensional parameters [14]. This is attributed to the fact that high responsivity requires the active region of PDs to be thick and long, which leads to lower bandwidth owing to high carrier transit time and high RC component, respectively. Since the BPD is a part of a coherent receiver, the later shows similar trade-offs among its output current and bandwidth. Travelling wave photodetectors (TW-PDs) can in principle achieve both the goals: high bandwidth and high responsivity [14]. But long TW-PDs lead to high RF losses [15]. Also, they are designed for a narrow wavelength range to attain velocity matching between optical and RF signals. Since we intend to develop the generic InP platform for a wide wavelength range, we have focused on lumped BPDs in our work which can be integrated with a widely tunable laser. Several research groups have tried to achieve detectors with bandwidth more than 100 GHz by engineering the layerstack [16], [17], [18]. But these approaches focus on stand-alone PDs and overlook generic integration. We target to optimize BPDs on a generic InP platform towards achieving the highest bandwidth for a particular responsivity, which depend on physical dimensions and layerstack [19], [20]. It is done by creating an equivalent circuit model of BPD and transforming various physical parameters to the corresponding circuit elements. Equivalent circuits are widely used in the electrical engineering as they are

more intuitive, easy to process and moderate in computation [21]. Parameters, that are specific to the generic platform are not tuned for BPD optimization e.g. number and thickness of quantum wells, material composition of quantum wells and barriers, wavelength of the incoming optical signal, contact resistance, material properties of the layerstack etc. We focus on achieving highest bandwidth at a responsivity by optimizing four physical parameters: length of each detector, thickness of core, position of MQW inside core, and barrier thickness between two QWs. These parameters impact RC parasitics and transit time of BPD, which in turn affect its bandwidth and responsivity, as discussed in section IV-C. An Opto-electronic transfer function is derived from the equivalent circuit and is used for all calculations. Conventional optimization of multiple parameters needs a lot of time. So, we employ Particle Swarm Optimization (PSO), a metaheuristic algorithm proposed by Kennedy and Ebarhart in 1995 in an attempt to model social interaction among school of fish or flock of birds [22]. PSO can generate high-quality solutions within shorter calculation time, which has a robust convergence characteristic compared to other heuristic algorithms such as ant colony optimization, simulated annealing, firefly algorithm, genetic algorithm etc. [23]. We also present how optimized BPD can be integrated with a laser using the same layerstack to implement a coherent receiver.

This article is organized as follows: section II presents the layerstack for BPD, and its device structure followed by its equivalent circuit model and the transfer function. DC and RF responsivity are presented in the section III. BPD optimization by PSO, power budget estimation of coherent receiver and strategy for integrating optimized BPD with laser are presented in section IV. Section V concludes the work.

II. MODELLING BACKGROUND

This section starts with the cross-section and device structure of waveguide PDs on our generic InP platform. We represent the BPD with an electrical circuit by translating various physical parameters into equivalent circuit components.

A. Device Structure of Single Detector

Waveguide-based detectors are considered for this work due to suitability of photonic integration. Besides, the length of the waveguide can be designed so that the majority of photons are absorbed without impacting the transit time [14], [19]. Fig. 1 shows the InP-based p-i-n heterostructure, used for designing the BPD. The core of the waveguide, containing the absorbing i-MQW, is sandwiched between p-InP and n-InP layers. Quantum wells (QWs) are made of $In_xGa_{1-x}As_yP_{1-y}$, whose compositions are chosen such that the bandgap emission wavelength remains at 1550 nm, also known as i-Q1.55. Our analysis holds for any composition of Q1.55 QWs. Different compositions and strain profiles of Q1.55 are listed in the work by Olsen et al. [24]. However, some of them might be easier to grow. Quantum barriers and the rest of the core is made of i-Q1.25 with bandgap emission of 1250 nm. The position of the MQW stack inside the core is represented with p-offset and n-offset, depicted in fig. 1. The width of a PD is expressed as W_{PD}. The thickness of the core
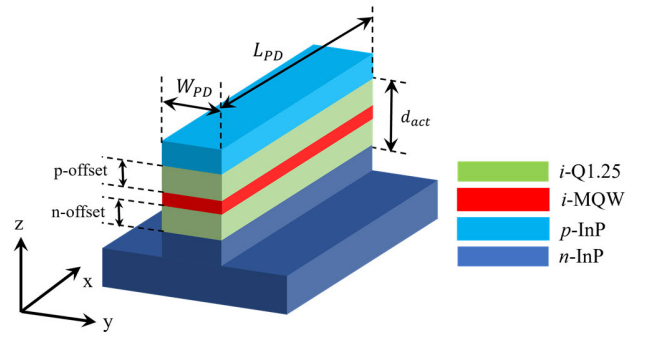

Fig. 1. Structure of the waveguide used for designing BPD. The Core comprises of absorbing i-MQW and two non-absorbing quaternary i-Q1.25 layers. Distance from p-InP and n-InP to i-MQW are termed as p-offset and n-offset, respectively. Width and length of each PD waveguide are shown as W_{PD} and L_{PD}, respectively.

is denoted as d_{act}, which has a lower bandgap and higher refractive index, while the cladding layers p-InP and n-InP have higher bandgap and lower refractive index. Such a profile in refractive index and bandgap help the optical mode to be confined in the core region. Schematic of a single detector structure is shown in fig. 2(a). Polyimide is used as a polymer to planarize the topological difference between p-metal and n-metal. Junction capacitance inside the PD is C'_j. Whereas, C_{poly} is the capacitance due to polyimide in between p-metal and n-InP. C_{poly} could be avoided if the width of p-metal is exactly the same as the width of PD waveguide. However, due to technological challenges, p-metal of width 5 μm is considered atop p-InP centered with the waveguide. C_{poly} can be a limiting factor for higher BPD bandwidth in case of poor planarization below p-metal, as areas with thinner polyimide leads to higher C_{poly}. We have considered perfect planarization for all the analysis. Generated electron-hole pairs in the MQW stack are separated by the electric field, present in the intrinsic region under reverse bias and are collected in the n-InP and p-InP layers, respectively. The equivalent circuit components for different regions are indicated in fig. 2(b), which are discussed in the below sub-section.

B. Equivalent Circuit Model of Balanced Detector

Schematic and equivalent circuit of BPD are shown in fig. 3. In case of waveguide based BPDs, optical modes with different phases (180° apart) get detected by two PDs. The difference current ($I_{out} = I_1 - I_2$) is extracted from the intersection of these PDs. I_1 and I_2 are the generated AC currents by the detectors PD_1 and PD_2, respectively. The phase difference between these two currents is 180° to reflect the phase difference of two optical signals onto PD_1 and PD_2. Fig. 3(b) shows the equivalent circuit model of a BPD. The active region of the PDs is represented with a junction resistance R_j and an effective junction capacitance $C_j(= C'_j || C_{poly})$ in parallel. Series resistance and load resistance are R_s and R_L, respectively. R_s is determined by the doping, thickness and dimensions of p-InP and n-InP. We only consider varying the area of p-InP for our analysis. As, R_s primarily depends on resistance from p-InP, it's approximated as $R_s \cong R'_s \times A'_{PD}/A_{PD}$. Here, A_{PD} is the top area of p-InP of waveguide PD under consideration and A'_{PD} is the corresponding area
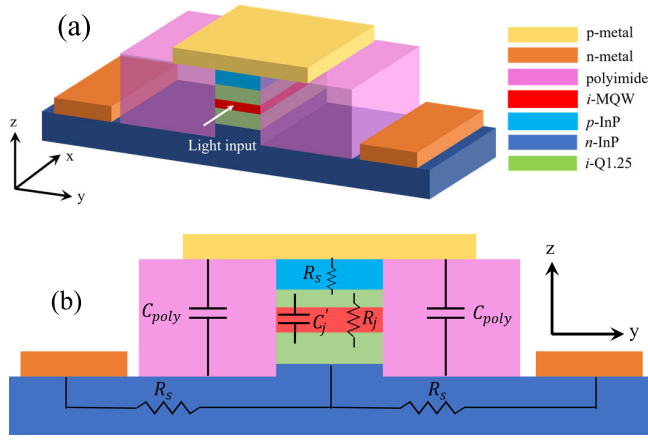
Fig. 2. (a) Structure of the detector. Light propagates in x-direction. Intrinsic core region, comprising MQW is sandwiched between p-InP and n-InP. Trenches of waveguide are filled with polyimide. The p-metal is deposited on top of p-InP and polyimide. (b) Cross-section view of the detector. Capacitive and resistive components are shown, which are described in the text. Both the schematics are not in scale.
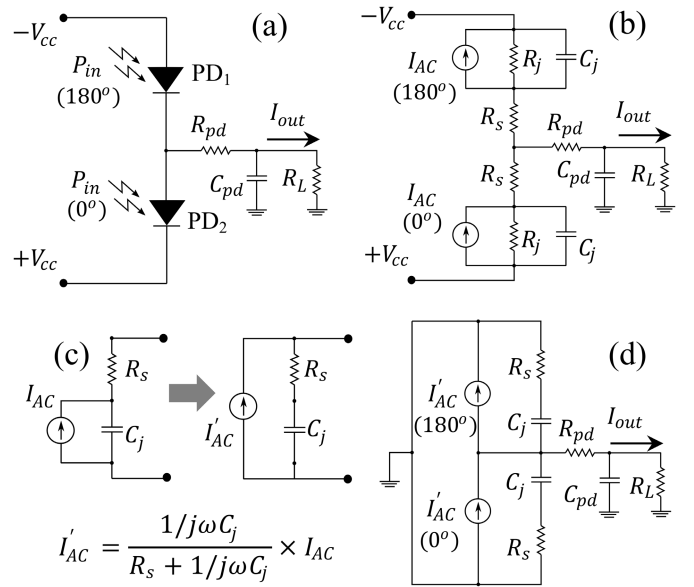

Fig. 3. (a) Schematic of a balanced detector. Light inputs are fed to two photodiodes separately. (b) Equivalent circuit for the balanced detector. (c) Norton equivalent circuit of the active region. Transfer function for the Norton equivalent current source is presented. (d) Equivalent circuit for AC analysis. DC voltage sources are shorted. (a,b,d) are adapted with permission from [25] ©The optical Society.

for reference PD with width 1.5 μm and length 50 μm. The series resistance of the reference PD is R'_s. Pad resistance R_{pd} arises because of carriers travelling through the metal tracks before getting collected by the probe, where the metal pad is considered to be just after the PD. R_{pd} depends on width, thickness and resistivity of the metal tracks. C_{pd} is the capacitance due to metal pads. The current source I_{AC} denotes the generated RF current during detection. The junction of the PDs can be converted with Norton equivalent circuit, as shown in fig. 3(c). Norton equivalent current I'_{AC} is computed and expressed in the figure. Junction impedance R_j is ignored because of very high values ($10-100$ MΩ) under reverse bias. Fig. 3(d) shows the AC equivalent circuit of the BPD by replacing the PD junction with Norton equivalent circuit and shorting the DC bias source.

III. BANDWIDTH AND RESPONSIVITY CALCULATION

The responsivity of a PD is defined as the amount of current generated with respect to DC optical power, denoted as R_{DC}, which can be expressed with the absorption coefficient of QWs in MQW detector. Whereas, bandwidth of a PD is defined as the frequency where its responsivity drops to 3 dB of R_{DC} [20]. We express the effective frequency-dependent responsivity $R(\omega)$ of BPD with two parts: (i) DC component to know the responsivity and (ii) AC component to compute its bandwidth. This section describes both the components of $R(\omega)$ and corelate them with the physical parameters of BPDs.

A. DC Responsivity

The DC component of responsivity R_{DC} for a waveguide-based PD depends on different parameters e.g. optical confinement, the distance travelled by light, the optical absorption at different regions and the photon energy. For a known waveguide structure, these parameters can be reliably simulated and/or measured. Absorbed light in the QWs contribute to the photocurrent. Free-carrier absorption of light in p-InP and n-InP regions results in heat generation through phonon

emission [26]. The light intensity drops exponentially as it travels through an absorbing material [27]. R_{DC} for a BPD of length L_{PD} can be expressed as:

$$R_{DC} = \frac{q}{\hbar\omega} \times e^{-\alpha_n \times \Gamma_n \times L_{PD}} \times e^{-\alpha_p \times \Gamma_p \times L_{PD}} \times \left(1 - e^{-\Gamma_{QW} \times \alpha_{QW} \times L_{PD}}\right) \quad (1)$$

Here, the length of BPD is denoted by L_{PD}. The photon energy of the input optical signal is denoted as $\hbar\omega$ and the electronic charge is q. Optical confinement in the QWs is denoted as Γ_{QW}. The absorption coefficient of input light for the corresponding wavelength in the QWs is α_{QW}. We consider only the internal responsivity of BPD. So, coupling loss is not considered in calculating R_{DC}. Absorption coefficients for n-InP and p-InP are denoted as α_n and α_p, respectively, which depend on the corresponding doping densities [28]. The optical confinement factors in n-InP and p-InP regions (excluding the extended depletion regions in reverse bias) are Γ_n and Γ_p, respectively.

B. Effective Responsivity

The effective responsivity $R(\omega)$ of a BPD depends on both the optical power and its frequency. It has both the DC (i.e. R_{DC}) and AC component. $R(\omega)$ can be expressed as:

$$R(\omega) = \frac{I_{out}}{P_{in}(\omega)} = \frac{I_{out}}{I'_{AC}} \times \frac{I'_{AC}}{I_{AC}} \times \frac{I_{AC}}{P_{in}(\omega)} \quad (2)$$

Three factors in the R.H.S. of equation (2) come from the equivalent circuit of BPD, shown in fig. 3(d). I_{out}/I'_{AC} is the output current gain with respect to Norton equivalent current. Gain ratio of Norton equivalent current to the original current is I'_{AC}/I_{AC} in fig. 3(c). These two factors possess information of the bandwidth due to RC loading. The ratio of

generated current to the incident optical power is $I_{AC}/P_{in}(\omega)$, that contains information

$$R(\omega) \propto \frac{\frac{1}{j\omega C_j}}{R_s + \frac{1}{j\omega C_j}} \times \frac{1}{1 + j\omega\tau} \times 2\left(R_s + \frac{1}{j\omega C_j}\right)$$
$$\times \frac{1/\left(1 + j\omega R_L C_{pd}\right)}{R_s + 2R_{pd} + \frac{2R_L}{1+j\omega R_L C_{pd}} + \frac{1}{j\omega C_j}} \quad (3)$$

of optical absorption in the QWs and bandwidth limitation due to the carrier transit time. By applying node analysis to the equivalent circuit, we solve I_{out}/I'_{AC}. Rate equations are solved in the active region to get an expression for $I_{AC}/P_{in}(\omega)$. So we get $R(\omega)$ as shown in equation (3). Elaborated calculations of $R(\omega)$ are described in Appendix A. We do not take DC parameters in the factor $I_{AC}/P_{in}(\omega)$ of equation (2) into account as they will be expressed as R_{DC}. For $\omega \rightarrow 0$, $R(\omega)$ must lead to R_{DC}. We thus normalize $R(\omega)$ for $\omega \rightarrow 0$ and express the effective responsivity as below:

$$R(\omega) = R_{DC} \times \frac{\frac{1}{j\omega C_j}}{R_s + \frac{1}{j\omega C_j}} \times \frac{1}{1 + j\omega\tau} \times \left(R_s + \frac{1}{j\omega C_j}\right)$$
$$\times \frac{1/\left(1 + j\omega R_L C_{pd}\right)}{R_s + 2R_{pd} + \frac{2R_L}{(1+j\omega R_L C_{pd})} + \frac{1}{j\omega C_j}} \quad (4)$$

The DC responsivity R_{DC} is calculated by applying $\omega \rightarrow 0$ in equation (4) and the bandwidth is calculated as the value of ω where $20\log_{10}|R(\omega)|$ drops by 3 dB. The effective transit time of carriers (τ_c) is included in the term τ. The bandwidth can be limited due to high τ_c or high RC value. Based on these reasons, BPD can either be in transit time limited or RC limited region, respectively. The transit time of electrons (τ_n) and holes (τ_p) are calculated as weighted average of optical confinement at i^{th} quantum well and time taken by carriers to travel from that well to the corresponding collecting layer:

$$\tau_n = \frac{\sum_i \left(\tau_i^n \times \Gamma_i\right)}{\sum_i \Gamma_i} \quad (5)$$

$$\tau_p = \frac{\sum_i \left(\tau_i^p \times \Gamma_i\right)}{\sum_i \Gamma_i} \quad (6)$$

Confinement of the optical mode in i^{th} well is Γ_i. Collection time for electrons and holes generated in the ith well are τ_i^n and τ_i^p, respectively. Throughout the paper, it is assumed that enough reverse bias is applied to the BPD so that the velocity of carriers saturates. The effective transit time (τ_c) can be computed from the effective saturation velocity of carriers in the active region. The saturation velocity (V_{sat}) can be expressed as [14]:

$$V_{sat} = \left(0.5 \times \left(\left(\frac{1}{V_{sat}^p}\right)^4 + \left(\frac{1}{V_{sat}^n}\right)^4\right)\right)^{-\frac{1}{4}} \quad (7)$$

Saturation velocity for electrons and holes are V_{sat}^n and V_{sat}^p, respectively. Considering effective transit time $\tau_c = d_{act}/V_{sat}$, we can get from equations (5)–(7):

$$\tau_c = \left(0.5 \times \left(\tau_p^4 + \tau_n^4\right)\right)^{\frac{1}{4}} \quad (8)$$

TABLE I

PARAMETERS FOR THE SIMULATION [14], [29]

Symbol	Description	Value
V_{sat}^p	saturation velocity of holes	6.6×10^4 m/s
V_{sat}^n	saturation velocity of electrons	2.6×10^5 m/s
E_{sat}	Electric field for velocity saturation	70 kV/cm
C_{pd}	pad capacitance	12 fF
W_{pm}	width of p-metal track	$5\ \mu m$
t	thickness of metal track	$1\ \mu m$
ρ	resistivity of metal track (gold)	2.35×10^{-8} Ω-m
ϵ_{act}	relative permittivity of active region	13
ϵ_0	permittivity of vacuum	8.854×10^{-12} F/m
ϵ_{poly}	relative permittivity of polyimide	2
n_{core}	Refractive index of core	3.38
n_{clad}	Refractive index of cladding	3.17
n_{poly}	Refractive index of polyimide	1.5
λ_0	wavelength in vacuum	1550 nm
α_{QW}	absorption coefficient of QWs	10^4 cm^{-1}
$\hbar$	Reduced Plank's constant	1.055×10^{-34} J-s
n_g	Group index	3.65
c_o	Speed of light in vacuum	3×10^8 m/s
τ_r	radiative lifetime	1 ns
d_{poly}	depth of polyimide	$2\ \mu m$
W_{PD}	width of detector	$1.5\ \mu m$
R'_s	series resistance of reference PD	20 Ω
R_L	load resistance	50 Ω
N_A	Doping density of p-InP cladding	10^{17} cm^{-3}
N_D	Doping density of n-InP cladding	10^{17} cm^{-3}
n.i.d	Non intentional n-doping of core	10^{16} cm^{-3}
QW	Quantum well thickness	5 nm

IV. RESULT AND DISCUSSION

This section starts with computing the confinement factor in the waveguide. We then present the bandwidth of BPDs and discuss bottlenecks to achieve high bandwidth due to various physical parameters. The dimensions we consider to tune are: width of the active region (d_{act}), length of the detector (L_{PD}), distance of MQWs from p-InP (p-offset) and quantum barrier thickness. Optimization of BPDs by our developed PSO-based algorithm is demonstrated for the above-mentioned physical parameters. A design methodology for a coherent receiver is also investigated. All simulation parameters are listed in table I.

A. Optical Confinement in Detectors

The responsivity in waveguide detectors greatly depends on the optical confinement along its physical dimensions. Here, we try to find out how optical confinement varies with width of the BPD (W_{PD}). Fig. 4(a−d) show the fundamental TE mode in the waveguide of detectors having a width (W_{PD}) of $1.5-3.0\ \mu m$ using LUMERICAL mode solver. Thickness of the core (d_{act}) is kept as 500 nm in all the cases. Insignificant change in the corresponding confinement factors (Γ_{2D}) shows that the optical field is well confined in y-direction for the above range due to large dimension and high contrast in refractive index. We choose this range because the lower limit of W_{PD} is defined by the generic technology. And, a very wide waveguide results in lossy higher order modes. But the optical confinement depends significantly on d_{act} for the range of $100-600$ nm as a lower contrast in refractive indices along
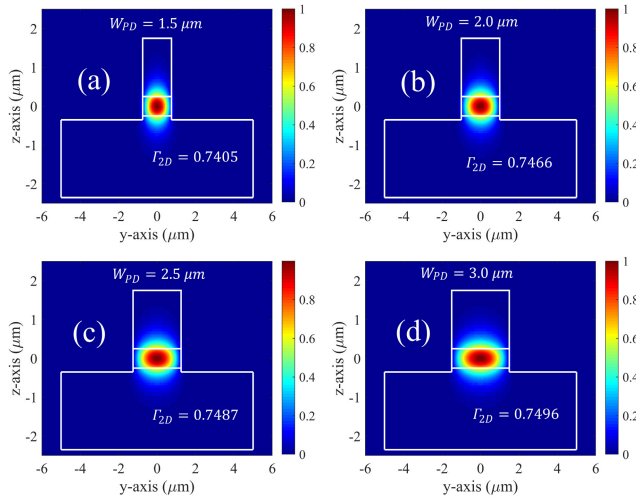
Fig. 4. (a−d) show fundamental TE mode for waveguide PDs with width (W_{PD}) in the range 1.5−3.0 μm. Corresponding confinement factors show insignificant change because of change in W_{PD} as optical confinement is already very high in y-direction.

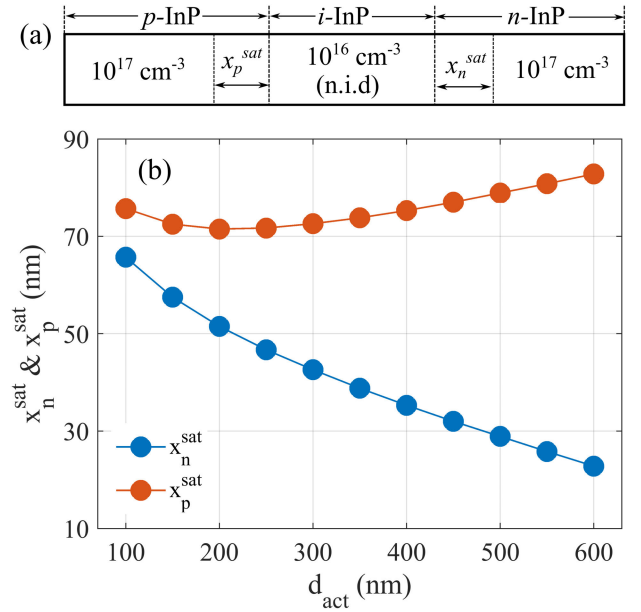

Fig. 5. (a) Schematic of a p-i-n diode with relevant doping densities. x_n^{sat} and x_p^{sat} are encroached depletion region in n-InP and p-InP layers, respectively for the reverse bias, required for velocity saturation. (b) x_n^{sat} decreases with increase in d_{act}. Whereas, x_p^{sat} shows slight increase.

the z-direction leads to leakage of light. We calculate the confinement factor for z-direction of PDs by solving Maxwell equations to find the profile of the fundamental TE mode [30]. Details of the equations are in Appendix B.

B. Calculation of Depletion Width

Calculating the depletion width is essential to find out the bandwidth of the detectors. The electric field of ∼70 kV/cm is required in the active region of InP/InGaAs detectors for velocity saturation of carriers [31]. The required reverse bias to attain the electric field leads to an extension of the depletion region beyond the intrinsic core region. We calculate the corresponding extension of the depletion region into the n-InP $\left(x_n^{sat}\right)$ and p-InP $\left(x_p^{sat}\right)$ layers through depletion approximation [32]. Fig. 5 shows that x_n^{sat} decreases significantly with d_{act}. Whereas, x_p^{sat} increases slowly after an initial dip. This implies lesser extension of the depletion region in p-i-n BPDs with thicker cores. We have taken x_n^{sat} and x_p^{sat} into account for calculating the junction capacitance and transit time of photogenerated carriers. Encroached depletion regions in p-InP and n-InP layers are excluded from the calculation of free-carrier absorption, as discussed in section III-A.

C. BPD Optimization

In order to optimize the BPD, we need to identify the effect of various parameters on the bandwidth and responsivity. Equation (4) is solved to calculate the bandwidth and responsivity. Fig. 6 shows the bandwidth for different p-offset and n-offset at different lengths (L_{PD}) of BPD. The thickness of the quantum barrier is considered as 10 nm in both the sub-figures. The core thickness (d_{act}) is varied by changing only the p-offset and n-offset, respectively. It can be observed from fig. 6(a) that depending on p-offset and L_{PD}, BPD falls into two regions: transit time limited regime because of higher values of p-offset and RC limited regime

due to higher capacitance from thinner p-offset. Also, a longer BPD leads to lower bandwidth. This comes from equation (4), as explained in section III. Fig. 6(b) shows that higher values of n-offset don't push the BPD into transit time limited regime unlike for the case of higher p-offset in fig. 6(a). Much faster electrons essentially keep the BPD in the RC limited region. The MQW stack is sufficiently close to p-InP for a p-offset of 50 nm. So, the slower holes cannot put the BPD into transit time limited regime. The evolution of BPD bandwidths with barrier thickness for different p-offset values is shown in fig. 7. L_{PD} is calculated at each datapoint to satisfy the responsivity of 1.0 A/W. For d_{act} = 400nm in fig. 7(a), p-offset of 50 nm places the MQW layerstack too close to the p-InP layer. In this case, confinement of the optical mode in the quantum wells is low for too thin or too thick quantum barrier, as the optical mode is mostly confined in the middle of the core (fig. 4). Thus, a longer BPD is required to achieve the desired responsivity, pushing the BPD into RC limited regime. However, p-offset of 150 and 200 nm means that the MQW stack is too far from p-InP, resulting in lesser bandwidth due to high transit time of slow holes. So, the highest bandwidth can be obtained for an optimum p-offset. A similar explanation can be deduced for fig. 7(b) in case of d_{act} = 600 nm and it is preferred that MQW stack stays close to p-InP to obtain high bandwidth irrespective of the core thickness (d_{act}). We can conclude from fig. 7 that the barrier layer between QWs should be of minimum thickness for the optical confinement factor to be maximum. However, it should be thick enough to prevent coupling between quantum wells [33]. So, we can tune the remaining three parameters (i.e. d_{act}, L_{PD}, and p-offset) to optimize a BPD, which is done through a PSO- based algorithm. Details of the algorithm are provided in the Appendix C and parameters are chosen accordingly [34].
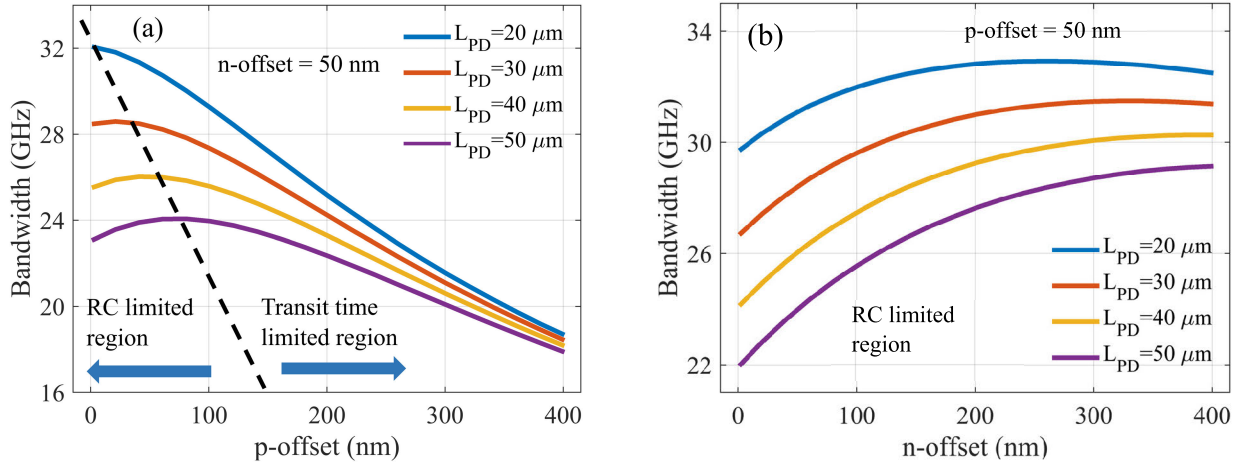
Fig. 6. (a) and (b) show bandwidth of BPD vs. p-offset and n-offset, respectively for different lengths of BPD. Higher p-offset is more likely to push the BPD into transit time limited regime as opposed to n-offset as holes are slower. Shorter BPD has higher bandwidth due to lesser RC value.
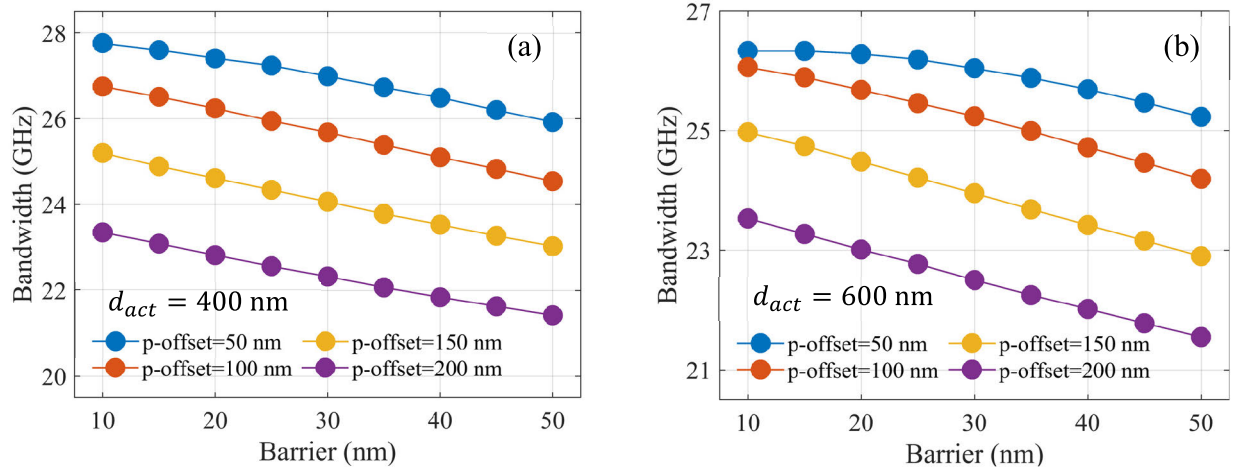

Fig. 7. Evolution of bandwidth of BPD with barrier thickness for different p-offset values. Length of the BPD is chosen to make responsivity to be 1.0 A/W at each data point. d_{act} is taken as 400 and 600 nm in (a) and (b), respectively. Highest bandwidth is achieved for the lowest barrier thickness at an optimum p-offset irrespective of d_{act}.

D. Optimization by PSO Algorithm

In order to design the BPD for the highest bandwidth at a given responsivity of 1.0 A/W, we choose 40 particles with random initial positions of three dimensions with reference to the three variables i.e. d_{act}, L_{PD} and p-offset within the user-defined solution space. The PSO algorithm calculates bandwidth and responsivity using equation (4) at each iteration. Every particle moves according to their position and velocity to check for the highest bandwidth if it has achieved the desired responsivity. The flowchart of the algorithm is presented in fig. 8. The standard deviations of three variables decrease with iterations indicating convergence of the particles, as shown in Fig. 9. The initial overshoot comes from a high particle velocity in order to make the search process effective. The algorithm is able to find the optimum BPD design depending on the trade-off between RC limited and transit time limited regions. Multiple combinations of design parameters are possible to achieve almost the same bandwidth at the same responsivity. Thus, the algorithm has a potential to provide different optimum designs of BPDs, as presented in

table II. Some of these designs are easier to grow or fabricate. The values of bandwidth and responsivity don't deviate much from their mean values for 10 samples, having standard deviations of ∼0.0422 GHz and ∼0.0008 A/W, respectively. Compared to a single *p-i-n* PD, the BPD suffers from reduced bandwidth due to two junction capacitances in parallel [35]. The last column of table II (i.e. Δ) indicates the distance from the *p*-InP layer to the midpoint of the MQW stack. Total thickess of the MQW stack is 50 nm. So, in all the cases, the MQW stack stays closer to the *p*-InP layer to get the highest bandwidth so that it is not limited by slower holes. Section IV-G dsicusses which of these BPD designs should be picked for designing coherent receiver.

E. Comparison With Other Optimization Algorithms

We have conducted a comparison of PSO with various other optimization techniques such as genetic algorithm (GA), firefly algorithm (FF) and simulated annealing (SA) in order to find the optimum design parameters of a BPD. We have run each algorithm 10 times and judge their quality by the average of

TABLE II

COMBINATION OF PARAMETERS BY PSO ALGORITHM

BW (GHz)	R (A/W)	d_{act} (nm)	L_{PD} (μm)	p-offset (nm)	Δ (nm)
27.8	1.0001	403.64	58.67	44.26	69.26
27.8	1.0007	368.12	58.27	33.68	58.68
27.7	1.0000	417.35	58.23	52.18	77.18
27.8	1.0002	381.94	56.84	45.63	70.63
27.8	1.0006	402.59	60.54	35.09	60.09
27.8	1.0018	348.52	58.34	26.80	51.80
27.8	1.0025	364.81	59.73	26.06	51.06
27.8	1.0004	354.02	58.17	29.70	54.70
27.7	1.0009	378.53	55.13	54.92	79.92
27.8	1.0004	396.75	58.40	43.17	68.17

TABLE III

COMPARISON OF VARIOUS OPTIMIZATION TECHNIQUES

Name	$\overline{BW}$ (GHz)	σ_{BW} (GHz)	$\bar{R}$ (A/W)	σ_R (A/W)	Time (sec)
PSO	27.78	0.0422	1.0008	0.0008	416.27
GA	27.57	0.0823	1.0053	0.0035	1958.16
FF	26.91	0.6574	1.0101	0.0102	1183.27
SA	-	-	-	-	-

$\overline{BW}$ = average of bandwidth, σ_{BW} = standard deviation of bandwidth, $\bar{R}$ = average responsivity, σ_R = standard deviation of responsivity
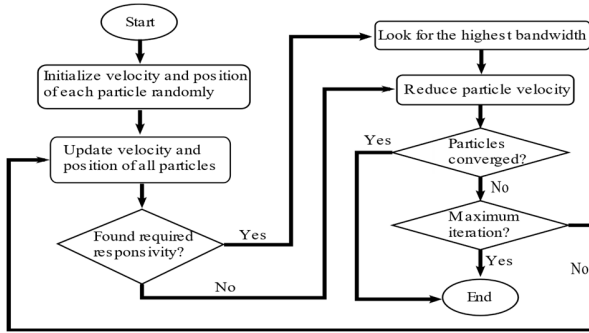

Fig. 8. Flowchart of the PSO algorithm to optimize BPDs. Particles are initialized with random position and velocity. Then each iteration updates their position and velocity to search for the highest bandwidth if the responsivity is already met. This process goes on until all the particles converge or maximum iteration reached.
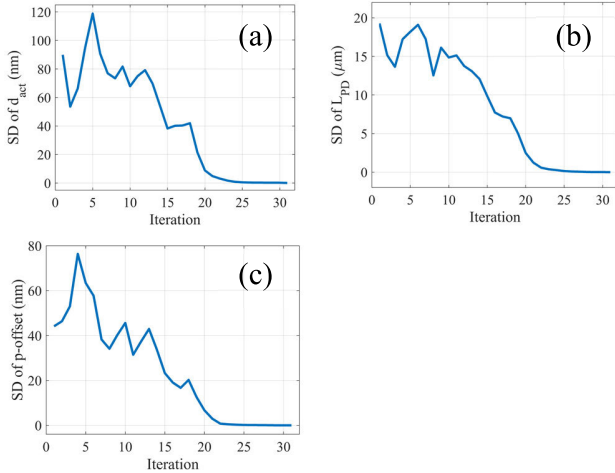

Fig. 9. (a−c) Standard deviations (SD) of d_{act}, L_{PD}, and p-offset with iterations. Simulation converges after 31 iterations in this case. High initial overshoot in the curves is due to high particle velocity set for the algorithm to have an extensive search.

highest achievable bandwidth and its standard deviation at a responsivity of 1 A/W. SA did not converge to solutions due to complex convergence criteria of the BPD. Table III shows that PSO leads to high-quality optimized designs in the shortest time. The reason is that PSO strikes a good balance between exploitation and exploration [36]. Particles explore the search space while exploiting the best-found solution by adjusting their velocities based on their own best positions and the global best position found by the swarm.

F. Bandwidth vs. Various Parameters

The optimum performance of a BPD has also been investigated for a number of parameters using the developed algorithm. In this sub-section, we only present the maximum possible bandwidth for a range of responsivities (R), width of the detector (W_{PD}) and absorption coefficient of QWs (α_{QW}) at the wavelength of 1550 nm. Optimum BPD designs (similar to table II) for each responsivity are not shown to keep the text simple. Fig. 10 shows that the highest bandwidth of BPD decreases with higher responsivity. This can be attributed to two requirements of higher responsivity: (i) longer detector, that increases RC value and (ii) thicker active region, leading to higher transit time. Fig. 11 shows that the highest bandwidth decreases with the width of the BPD. This is because of a higher contribution of the junction capacitance $\left(C'_j\right)$ to effective capacitance (C_j) as permittivity of the core region is higher than that of polyimide. So, BPDs with narrow waveguides give high bandwidths due to lesser capacitance. But, it is subject to technological limitations and high optical scattering due to sidewall roughness [37]. The lowest value of W_{PD} (1.5 μm) corresponds to the highest C_{poly} of ~1.55 fF, which is not too large to hamper BPD bandwidth significantly. The QW design can be engineered to get stronger absorption. So, we run the algorithm to determine how the absorption coefficient of QWs (α_{QW}) affects the performance of BPD, as shown in fig. 12. Increase of the highest bandwidth with α_{QW} is due to the fact that higher α_{QW} allows shorter detector for the same responsivity. It makes the BPD less impacted by RC loading. In both the cases of figure 11 and 12, changes are more noticable for lower bandwidths.

G. Coherent Receiver Design: A Case Study

This work aims to optimize the BPD for a coherent receiver on the generic InP platform, as mentioned in section I. Fig. 13 shows a simple schematic of a photonic integrated circuit (PIC) as part of a coherent balanced receiver [6], [38], [39]. The optical power of laser and input are denoted as L and S, respectively. We focus on a heterodyne coherent receiver as it is less affected by phase noise and is suitable for complex modulation schemes such as QAM and DPSK [40]. Control signals of the laser and the phase shifter come from a phase-locked loop (PLL) and are not shown here. The difference current of two detectors in a BPD of the coherent receiver is further processed by a transimpedance amplifier (TIA), which demands a certain amount of current
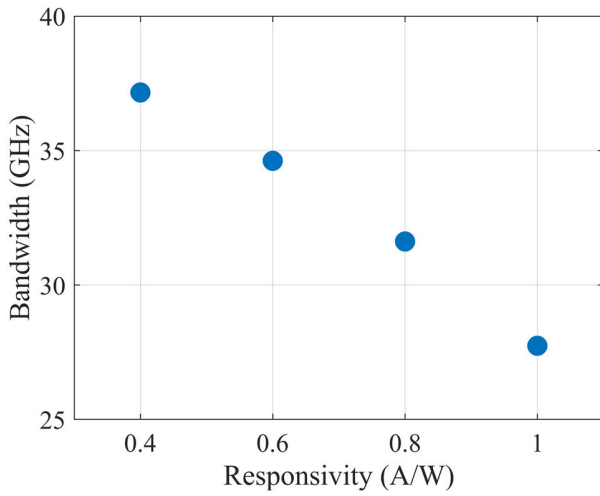
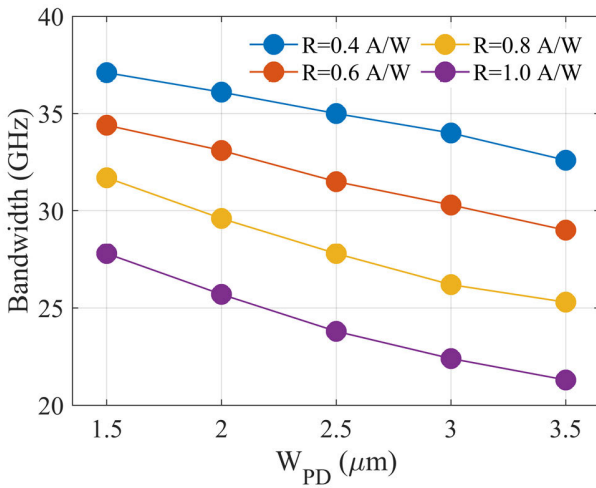Fig. 10. Highest bandwidth of BPD vs. responsivity values.

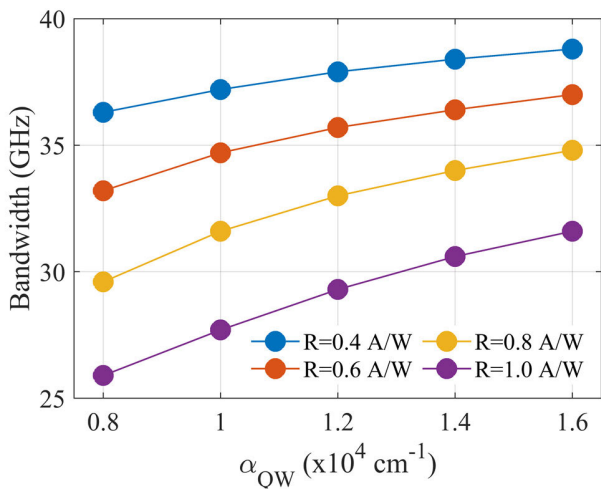Fig. 11. Highest bandwidth of BPD vs. BPD width (W_{PD}) for different values of responsivity (R).

Fig. 12. Highest bandwidth of BPD vs. absorption coefficient of QWs (α_{QW}) for different values of responsivity (R).
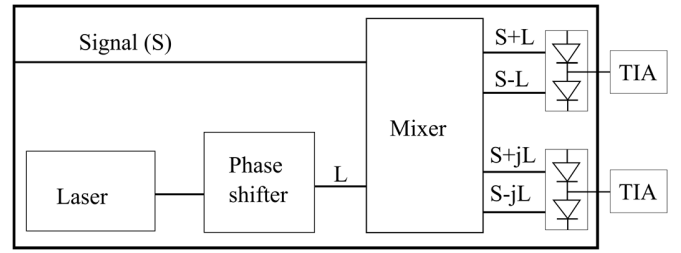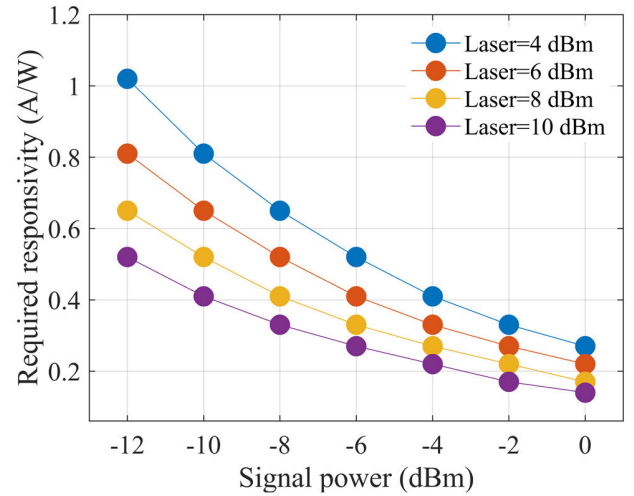

Fig. 13. Simple schematic of a coherent balanced receiver.

Fig. 14. Required responsivity of balanced detector in the coherent receiver. It increases for low signal power and/or low laser power.

from the BPD for successful detection. This depends on the power level of input signal, laser output, responsivity of the BPD and losses in the circuit. The minimum required output current of BPD is considered to be 160 μA_{pp} (difference of current between positive and negative maxima), which aligns with linear TIAs, investigated by Awny et al. [41]. The input signal and laser output are mixed in a 90º hybrid coupler and four output signals are then fed to the two sets of BPDs. The phases of two optical signals, going to a pair of detectors in a BPD are 180º apart [6], [38], [39]. The resultant photocurrent of each PD is directly related to the square of effective incident electric field [40]. The required responsivity of BPDs to meet the minimum current requirement of TIAs for a range of input powers are shown in fig. 14 for different laser power levels. Appendix D provides the methodology for this calculation. For a higher laser and/or signal power, required responsivity of BPD goes lower. This can lead to a higher bandwidth, as demonstrated in figure 10. But, there is a limit in laser power to prevent thermal runaway, detector nonlinearity, saturation of output current, violation of power handling limit by the PDs. The input optical power is considered to be the lowest value expected during the operation of receiver. So, we need to optimize the design parameters of BPD for a certain combination of laser and input power while considering all lossy elements of the receiver circuit.

The developed PSO algorithm is able to produce several optimized BPD designs. To realize the coherent receiver, we need to find out which of these designs can be monolithically integrated with the laser, that works as the local oscillator. Let's consider a scenario, where we know the threshold current for lasing I_{th}, laser power at a corresponding driving current and position of MQW stack in the waveguide core on the generic platform. The power budget estimation of coherent
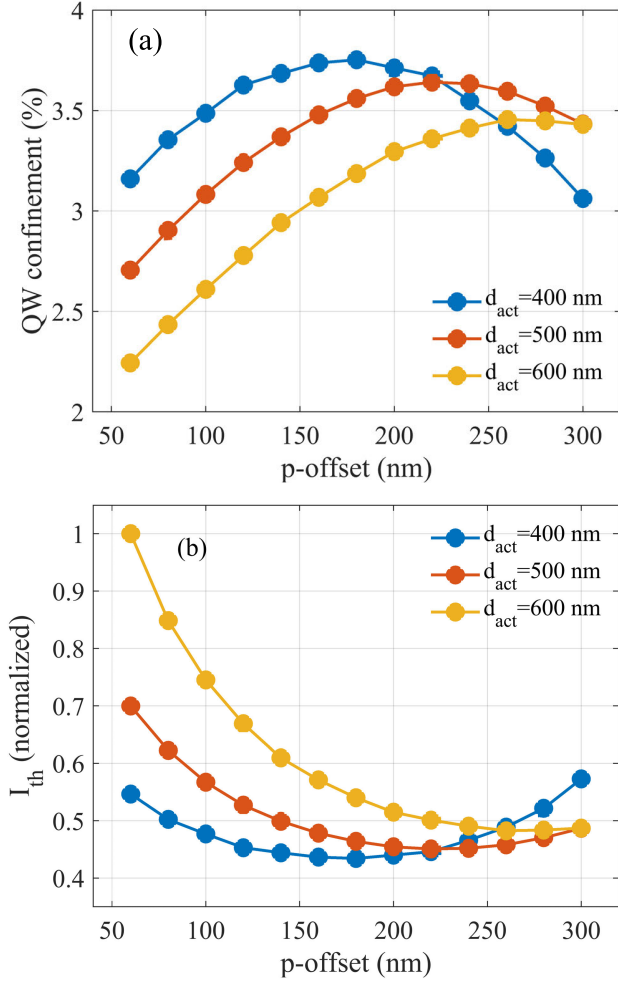
Fig. 15. Optical confinement in QWs is the highest and threshold current of laser (I_{th}) is at its minimum if the MQW stack is in the middle of active region, shown in (a) and (b), respectively.
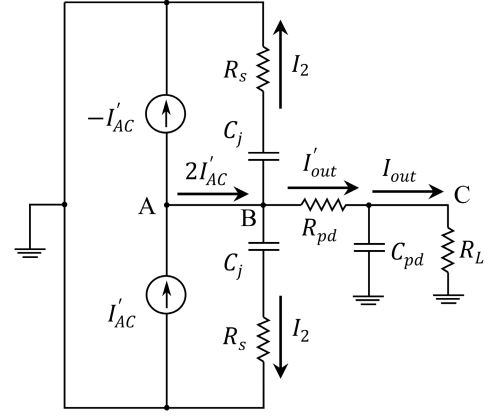

Fig. 16. Equivalent circuit of BPD for AC analysis. Relations between current components through different branches are in the text.

at the onset of lasing. It is considered that the injected current is not too high and laser operates in linear region. Total cavity loss is denoted as α_L. Higher current injection is needed to fulfil the equation (9) for lower Γ_{QW}, which increases the threshold current. Since laser power increases linearly with $I - I_{th}$, it will also decrease with higher I_{th} when the MQW stack deviates from the middle of core region. Appendix E provides details of this simulation. Together with fig. 15(b) and the measured laser power, the developed PSO-based algorithm will be able to indicate which of the optimized BPD designs should be implemented in the generic platform while making sure of the required laser power for the coherent receiver.

V. CONCLUSION

To conclude, we have developed a design methodology to optimize MQW BPDs on generic InP platform through a PSO-based algorithm using its equivalent electrical circuit. We have designed BPDs for the highest bandwidth possible at a given responsivity while making sure of compatibility to generic integration. The impact of different physical parameters on BPD's performance are thoroughly investigated and strategies to circumvent major bottlenecks have been identified. Quantum barriers must be as thin as possible without leading to coupling of QWs. Values of corresponding design parameters i.e. length and width of BPD, and core thickness are optimized via the PSO algorithm. The highest bandwidth increases with lower responsivity, thinner detectors and higher absorption coefficient of QWs. The MQW stack should be closer to p-InP layer to achieve high bandwidth by overcoming the bottleneck of slower holes. But, using the same layerstack of BPDs for lasers leads to higher threshold current for lasing. So, a trade-off has to be made, which is presented in a case study of designing a coherent receiver on generic InP platform.

APPENDIX

A. Deriving Components of $R(\omega)$

Fig. 16 shows the equivalent circuit of BPD for AC analysis along with current components through different branches.

receiver tells us how much of laser power can be reduced and the corresponding required BPD responsivity, as presented in section II-A. The required responsivity of BPD must be within the theoretical limit at the wavelength of input optical signal (e.g. 1.25 A/W for 1550 nm). Combinations of different p-offset and d_{act} for BPD shall be determined through the algorithm for the highest bandwidth at that required responsivity. Considering the same layerstack for laser, the threshold current for lasing (I_{th}) can then be calculated for a specific set of p-offset and d_{act}. Here, we calculate I_{th} and the optical confinement in QWs for a wide range of p-offset at different d_{act}. The simulation parameters are taken from previous works on generic platform [42], [43]. Table II shows that MQW should be closer to p-InP for an optimum BPD. But it degrades confinement in the QWs, which increases the threshold current for lasing, as shown in fig. 15. It can be explained with the following condition for lasing [13]:

$$\Gamma_{QW} g(I) - \alpha_L = 0 \qquad (9)$$

Optical confinement factor of QWs is Γ_{QW}. Material gain is $g(I)$ which is dependent on driving current I and gets clamped

Analyzing KCL and KVL at node B and C give us:

$$I'_{out} = 2I'_{AC} - 2I_2 \tag{10}$$

$$I'_{out} \times \left(R_{pd} + \frac{R_L}{1 + j\omega R_L C_{pd}} \right) = I_2 \times \left(R_s + \frac{1}{j\omega C_j} \right) \tag{11}$$

$$I_{out} = \frac{1/j\omega C_{pd}}{R_L + 1/j\omega C_{pd}} \times I'_{out} \tag{12}$$

Solving equations (10)−(12) gives:

$$\frac{I_{out}}{I'_{AC}} = \frac{2\left(R_s + \frac{1}{j\omega C_j} \right)/(1 + j\omega R_L C_{pd})}{R_s + 2R_{pd} + \frac{2R_L}{1 + j\omega R_L C_{pd}} + \frac{1}{j\omega C_j}} \tag{13}$$

In order to find out the term I_{AC}/P_{in} of equation (1), we need to consider dynamic behavior of the PD. Carrier dynamics in the PD can be expressed with the following rate equation:

$$\frac{dn}{dt} = Gn_0 P - \frac{n}{\tau} \tag{14}$$

The 1st term on R.H.S. is generation rate of carriers, which depends on intrinsic carrier density (n_0), photon density (P) and generation coefficient G. The 2nd term is the carrier removal rate, where τ is expressed as,

$$\frac{1}{\tau} = \frac{1}{\tau_c} + \frac{1}{\tau_r} \tag{15}$$

Here, τ_c is the carrier transit time after generation through applied electric field and τ_r is the recombination lifetime. We express photocurrent in terms of carrier sweep-out rate as,

$$I_{AC} = \frac{qnV}{\tau_c} \tag{16}$$

Here, q is the electronic charge and V is the volume of active region. From the equations (14)−(16),

$$\tau \times \frac{dI_{AC}}{dt} + I_{AC} = \frac{qV\tau Gn_0 P}{\tau_c} \tag{17}$$

Considering $I_{AC} = I_0 \times \exp(j\omega t)$, equation (17) can be expressed as:

$$I_{AC} = \frac{qV\tau Gn_0 P}{(1 + j\omega\tau)\tau_c} \tag{18}$$

Considering that photon density P is linearly dependent on input optical power P_{in}, it can be written from equation (18):

$$\frac{I_{AC}}{P_{in}(\omega)} \propto \frac{1}{1 + j\omega\tau} \tag{19}$$

B. Calculating Optical Confinement in Waveguide

Electric field profile for TE mode along z-direction (see fig. 1) is calculated from the formula:

$$\frac{d^2E_z}{dy^2} + \left[k_0^2 n^2(z) - \beta^2 \right] E_z = 0 \tag{20}$$

Here, β is propagation constant, $n(z)$ is the refractive index profile along z-direction and k_0 is the wavenumber. Optical confinement in the QWs is calculated as:

$$\Gamma_z = \frac{\int_{QW} |E_z|^2 \, dz}{\int_{-\infty}^{\infty} |E_z|^2 \, dz} \tag{21}$$

C. Implementing Particle Swarm Optimization

Velocity and position of each particle are updated as per the following formulae:

$$V_{d,L}(i+1) = w \times V_{d,L}(i) + C_1 \left(P_{best}^{d,L} - P_{d,L}(i) \right)$$
$$+ C_2 \left(G_{best}^{d,L} - P_{d,L}(i) \right) \tag{22}$$

$$P_{d,L}(i+1) = P_{d,L}(i) + V_{d,L}(i) \tag{23}$$

The first term on R.H.S of equation (22) depends on already existent velocity of the particle. Second term is the velocity component driven by the particle's best position so far. And the third term is determined by the best find so far by the whole swarm. The parameter w is inertia coefficient, C_1 is cognitive coefficient and C_2 is social coefficient. P_{best} is the personal best position of the corresponding particle and G_{best} is the global best position found by the swarm so far. The values of w and C_1 are reduced after every iteration by a damping factor $(f_{damp} < 1)$ as $w(\text{or } C_1) = w(\text{or } C_1) \times f_{damp}$. The value of C_2 remains undamped, otherwise we observe particles to freeze after a few iterations. Damping only w and C_1 make sure that the whole swarm converges towards the global best.

D. Calculations for Heterodyne Coherent Receiver

The optical field associated with input signal and laser output can be expressed as:

$$E_s = A_s \exp\left[-i(\omega_0 t + \phi_s) \right] \tag{24}$$

$$E_{LO} = A_{LO} \exp\left[-i(\omega_{LO} t + \phi_{LO}) \right] \tag{25}$$

A_s, ω_0 and ϕ_s represent amplitude, frequency and phase of input signal, respectively. Whereas, the same parameters for laser are A_{LO}, ω_{LO} and ϕ_{LO}, respectively. The optical power on PDs is $P = K|E_s + E_{LO}|^2$, where $K = 0.5 \times \sqrt{\epsilon_0 \epsilon_r / \mu_0} \times A_{WG}$. Area of the cross-section of PD waveguide is A_{WG}. So, P can be expressed as:

$$P(t) = P_s + P_{LO} + 2\sqrt{P_s P_{LO}} \cos(\omega_{IF} t + \phi_s - \phi_{LO}) \tag{26}$$

$P_s = KA_s^2$, $P_{LO} = KA_{LO}^2$ and $\omega_{IF} = \omega_0 - \omega_{LO}$. We consider $\omega_{IF} = 1$ GHz for heterodyne receiver. Phase difference i.e. $|\phi_s - \phi_{LO}|$ will be maintained through the phase shifter and

$$\Gamma = \Gamma_{QW} \times \frac{L_{SOA}}{L_{SOA} + L_{passive}} \tag{27}$$

$$\alpha_m = \frac{1}{L_{SOA} + L_{passive}} \log\left(\frac{1}{\sqrt{R_1 R_2}} \right) \tag{28}$$

$$\alpha_i = \frac{\alpha_{SOA} L_{SOA} + \alpha_{passive} L_{passive} + \alpha_{excess}}{L_{SOA} + L_{passive}} \tag{29}$$

$$v_g = c_0 / n_g \tag{30}$$

$$g'_{0N} = \frac{g_0}{1 + g_c N_p} \tag{31}$$

$$g_{th} = (\alpha_i + \alpha_m) / \Gamma \tag{32}$$

$$N_{th} = N_{tr} \times \exp\left(\frac{g_{th}}{g'_{0N}} \right) \tag{33}$$

TABLE IV
PARAMETERS FOR THE SIMULATION [42], [43]

Symbol	Description	Value
L_{SOA}	Length of SOA	500 μm
$L_{passive}$	Length of passive section	1500 μm
R_1	Reflectivity rear mirror	0.92
R_2	Reflectivity of front mirror	0.85
α_{SOA}	Internal loss of SOA	25 cm^{-1}
$\alpha_{passive}$	Loss of passive section	3 dB/cm
α_{excess}	Excess loss in the cavity	3 dB
g_0	Material gain of SOA	2200 cm^{-1}
N_{tr}	Transparent carrier density	5x10^{17} cm^{-3}
B	Radiative recombination coefficient	2.6x10^{-10} cm^{3}s^{-1}
C	Auger recombination coefficient	1.4x10^{-28} cm^{6}s^{-1}
g_c	Gain saturation factor	5x10^{-17} cm^3
η	Carrier injection efficiency	0.80

$$I_{th} = \frac{qV}{\eta} \times \left(BN_{th}^2 + CN_{th}^3 \right) \tag{34}$$

$$N_p = \frac{\eta (I - I_{th})}{q v_g g_{th} V} \tag{35}$$

considered to be $\pi/2$ in our case. Current output of a PD is $RP(t)$, where R is responsivity. Current of BPD is defined as the difference currents of two PDs with a 180° phase difference. Propagation losses for input signal and laser for our platform are considered for calculations.

E. Calculating Threshold Current for Lasing

Equations (27)−(35) have been solved to calculate threshold current of laser I_{th} [13], [42]. Equations (31)−(35) have been solved self-consistently to obtain values for I_{th} and generated photon density N_p. Descriptions of parameters in the equations are provided in table IV. Effective optical confinement in the SOA is Γ. Mirror loss and average internal losses are calculated in the equations (28) and (29), respectively. Group velocity is v_g. Effective cavity gain is g'_{0N} which reduces due to very high N_p, defined by a gain saturation factor g_c. Threshold gain and the corresponding threshold carrier density are g_{th} and N_{th}, respectively. V is the volume of active medium i.e. QWs. The threshold current for lasing I_{th} doesn't show change even for a driving current of 200 mA. This is because $1 + g_c N_p \cong 1$ and the denominator in equation (31) remains almost unchanged.

REFERENCES

[1] L. T. Nichols, K. J. Williams, and R. D. Estman, "Optimizing the ultrawide-band photonic link," *IEEE Trans. Microw. Theory Techn.*, vol. 45, no. 8, pp. 1384–1389, Aug. 1997.

[2] M. Saiful Islam et al., "Distributed balanced photodetectors for broadband noise suppression," *IEEE Trans. Microw. Theory Techn.*, vol. 47, no. 7, pp. 1282–1288, Jul. 1999.

[3] C. B. Albert, C. Huang, and E. H. W. Chan, "Intensity noise suppression using dual-polarization dual-parallel modulator and balanced detector," *IEEE Photon. J.*, vol. 10, no. 2, pp. 1–8, Apr. 2018.

[4] X. Wang, N. Wada, T. Miyazaki, and K. Kitayama, "Coherent OCDMA system using DPSK data format with balanced detection," *IEEE Photon. Technol. Lett.*, vol. 18, no. 7, pp. 826–828, Apr. 1, 2006.

[5] A. H. Gnauck and P. J. Winzer, "Optical phase-shift-keyed transmission," *J. Lightw. Technol.*, vol. 23, no. 1, pp. 115–130, Jan. 2005.

[6] Y. Painchaud, M. Poulin, M. Morin, and M. Têtu, "Performance of balanced detection in a coherent receiver," *Opt. Exp.*, vol. 17, no. 5, pp. 3659–3672, Mar. 2009.

[7] D. Maes et al., "High-speed uni-traveling-carrier photodiodes on silicon nitride," *APL Photon.*, vol. 8, no. 1, Jan. 2023, Art. no. 016104.

[8] Y. Gao et al., "High-speed normal-incidence p-i-n InGaAs photodetectors grown on silicon substrates by MOCVD," *IEEE Photon. Technol. Lett.*, vol. 24, no. 4, pp. 237–239, Feb. 2012.

[9] H.-G. Bach et al., "InP-based waveguide-integrated photodetector with 100-GHz bandwidth," *IEEE J. Sel. Topics Quantum Electron.*, vol. 10, no. 4, pp. 668–672, Aug. 2004.

[10] M. Smit et al., "An introduction to InP-based generic integration technology," *Semicond. Sci. Technol.*, vol. 29, no. 8, Jun. 2014, Art. no. 083001.

[11] L. Xu et al., "High-performance InP-based photodetector in an amplifier layer stack on semi-insulating substrate," *IEEE Photon. Technol. Lett.*, vol. 20, no. 23, pp. 1941–1943, Nov. 2008.

[12] L. M. Augustin et al., "InP-based generic foundry platform for photonic integrated circuits," *IEEE J. Sel. Topics Quantum Electron.*, vol. 24, no. 1, pp. 1–10, Jan. 2018.

[13] L. A. Coldren, S. W. Corzine, and M. L. Mashanovitch, *Diode Lasers and Photonic Integrated Circuits*. Hoboken, NJ, USA: Wiley, Mar. 2012.

[14] G. Ghione, *Semiconductor Devices for High-Speed Optoelectronics*. Cambridge, U.K.: Cambridge Univ. Press, Oct. 2009, ch. 4.

[15] M. S. Islam et al., "High power and highly linear monolithically integrated distributed balanced photodetectors," *J. Lightw. Technol.*, vol. 20, no. 2, pp. 285–295, Feb. 2002.

[16] J. W. Shi, Y. S. Wu, C. Y. Wu, P. H. Chiu, and C. C. Hong, "High-speed, high-responsivity, and high-power performance of near-ballistic uni-traveling-carrier photodiode at 1.55-μm wavelength," *IEEE Photon. Technol. Lett.*, vol. 17, no. 9, pp. 1929–1931, Sep. 2005.

[17] D. H. Jun, J. H. Jang, I. Adesida, and J. I. Song, "Improved efficiency-bandwidth product of modified uni-traveling carrier photodiode structures using an undoped photo-absorption layer," *Jpn. J. Appl. Phys.*, vol. 45, no. 4S, p. 3475, Apr. 2006.

[18] Y. Liu et al., "High responsivity evanescently coupled waveguide photodiode using spot-size converter and distributed Bragg reflector at 1.55μm wavelength," *Infr. Phys. Technol.*, vol. 130, May 2023, Art. no. 104619.

[19] P. Runge et al., "Waveguide integrated balanced photodetectors for coherent receivers," *IEEE J. Sel. Topics Quantum Electron.*, vol. 24, no. 2, pp. 1–7, Mar. 2018.

[20] A. Beling and J. C. Campbell, "InP-based high-speed photodetectors," *J. Lightw. Technol.*, vol. 27, no. 3, pp. 343–355, Feb. 2009.

[21] P. S. R. Murthy, *Power Systems Analysis*. Oxford, U.K.: Butterworth-Heinemann, Jun. 2017, ch. 9.

[22] J. Kennedy and R. Eberhart, "Particle swarm optimization," in *Proc. IEEE ICNN*, vol. 4, Nov./Dec. 1995, pp. 1942–1948.

[23] K. Y. Lee and J. B. Park, "Application of particle swarm optimization to economic dispatch problem: Advantages and disadvantages," in *Proc. IEEE PES Power Syst. Conf. Expo.*, Oct./Nov. 2006, pp. 188–192, Oct. 2006.

[24] G. H. Olsen, T. Z. Zamerowski, R. T. Smith, and E. P. Bertin, "InGaAsP quaternary alloys: Composition, refractive index and lattice mismatch," *J. Electron. Mater.*, vol. 9, pp. 977–987, Nov. 1980.

[25] D. Nag, W. Yao, J. J. Van Der Tol, and K. A. Williams, "Investigating RC and transit time limited bandwidth of integrated balanced detectors through an equivalent circuit model," in *Optical Devices and Materials for Solar Energy and Solid-state Lighting*. Maastricht, The Netherlands: Optica Publishing Group, Optica, Jul. 2022, p. JTu2A-40.

[26] C. Kittel, *Introduction to Solid State Physics*. Hoboken, NJ, USA: Wiley, 2005.

[27] J. Piprek, *Semiconductor Optoelectronic Devices: Introduction to Physics and Simulation*. Amsterdam, The Netherlands: Elsevier, Oct. 2013.

[28] U. Khalique, "Polarization based integration scheme (POLIS)," Ph.D. dissertation, Dept. Electr. Eng., Tech. Univ. Eindhoven, Eindhoven, The Netherlands, 2008, ch. 2.

[29] L. Xu, "Monolithic integrated reflective transceiver in indium phosphide," Ph.D. dissertation, Dept. Electr. Eng., Tech. Univ. Eindhoven, Eindhoven, The Netherlands, 2009, ch. 5.

[30] M. N. Sadiku and S. Nelatury, *Elements of Electromagnetics*. New York, NY, USA: Oxford Univ. Press, 2001, ch. 10.

[31] S. Adachi, *Properties of Group-IV, III-V and II-VI Semiconductors*. Chichester, U.K.: Wiley, 2005.

[32] R. F. Pierret, *Semiconductor Device Fundamentals*. London, U.K.: Pearson, 1996, ch. 5.

[33] B. R. Nag, *Physics of Quantum Well Devices*. Dordrecht, The Netherlands: Kluwer, Nov. 2001.

[34] W. Zhang, H. Li, Q. Zhao, and H. Wang, "Guidelines for parameter selection in particle swarm optimization according to control theory," in *Proc. 5th Int. Conf. Natural Comput.*, vol. 3, Aug. 2009, pp. 520–524.

[35] A. Beling et al., "High-speed balanced photodetector module with 20 dB broadband common-mode rejection ratio," in *Proc. Opt. Fiber Commun. Conf.*, Mar. 2003, p. WF4.

[36] O. Olorunda and A. P. Engelbrecht, "Measuring exploration/exploitation in particle swarms using swarm diversity," in *Proc. IEEE Congr. Evol. Comput. (IEEE World Congr. Comput. Intelligence)*, Jun. 2008, pp. 1128–1134.

[37] Y. Wang, M. Kong, Y. Xu, and Z. Zhou, "Analysis of scattering loss due to sidewall roughness in slot waveguides by variation of mode effective index," *J. Opt.*, vol. 20, no. 2, Jan. 2018, Art. no. 025801.

[38] I. Kaminow, T. Li, and A. E. Willner, *Optical Fiber Telecommunications VB: Systems and Networks*. Amsterdam, The Netherlands: Elsevier, Jul. 2010, ch. 3.

[39] K. Kikuchi, "Fundamentals of coherent optical fiber communications," *J. Lightw. Technol.*, vol. 34, no. 1, pp. 157–179, Jan. 1, 2016.

[40] G. P. Agrawal, *Fiber-Optic Communication Systems*. Hoboken, NJ, USA: Wiley, Feb. 2012, ch. 10.

[41] A. Awny et al., "A linear differential transimpedance amplifier for 100-Gb/s integrated coherent optical fiber receivers," *IEEE Trans. Microw. Theory Techn.*, vol. 66, no. 2, pp. 973–986, Feb. 2018.

[42] S. Andreou, "Integrated stabilized laser systems for high resolution strain sensing," Ph.D. dissertation, Dept. Electr. Eng., Tech. Univ. Eindhoven, Eindhoven, The Netherlands, 2020, ch. 2.

[43] D. Pustakhod, K. Williams, and X. Leijtens, "Fast and robust method for measuring semiconductor optical amplifier gain," *IEEE J. Sel. Topics Quantum Electron.*, vol. 24, no. 1, pp. 1–9, Jan. 2018.

Weiming Yao (Member, IEEE) received the B.Sc. degree in electrical engineering from Technical University Berlin in 2010, the joint M.Sc. degree in photonic networks engineering from Aston University, U.K., and Scuola Superiore Sant'Anna, Italy, in 2012, and the Ph.D. degree from Eindhoven University of Technology (TU/e), in 2017, with a focus on integrated high-capacity optical transceivers. Since 2012, he has been with the Photonic Integration Group (PhI), TU/e. From 2017 to 2019, he was with the Photonic Integration Technology Centre (PITC), where he led an open innovation development project for fabrication of photonic ICs (OpenPICs) and was co-applicant in the EU InPulse Pilot line project. His research interests include high-speed and high-density photonic components, its integration with electronics, and neuromorphic photonics. Since 2020, he has been an Assistant Professor with TU/e after being awarded with the Dutch NWO Veni Grant for research on optical spiking neurons.

Dhiman Nag received the Bachelor of Engineering (B.E.) degree in electronics and communication from the University Visvesvaraya College of Engineering, India, in 2013, the Master of Technology (M.Tech.) degree in VLSI design and embedded systems from the R.V. College of Engineering, India, in 2015, and the Ph.D. degree from the Indian Institute of Technology Bombay (IITB), India, in 2021, with a focus on combating green gap in InGaN opto-electronics: from material to device perspective. He is currently working as a Post-Doctoral Researcher with the Photonic Integration Group (PHI), Eindhoven University of Technology (TU/e), The Netherlands. He is involved in modeling and designing of coherent receiver from component to circuit level. He was awarded the Visvesvaraya Fellowship to pursue the Ph.D. degree from IITB, in 2016. He received the "Naik and Rastogi Award for Excellence in Ph.D. Research."

Jos J. G. M. van der Tol received the M.Sc. and Ph.D. degrees in physics from the State University of Leiden, Leiden, The Netherlands, in 1979 and 1985, respectively. In 1985, he joined KPN Research, where he became involved in research on integrated optical components for use in telecommunication networks. Furthermore, he has been working on guided wave components on III–V semiconductor materials. He has also been active in the field of optical networks, focusing on survivability, introduction scenarios, and management issues. In July 1999, he was appointed as an Associate Professor with the Eindhoven University of Technology, Eindhoven, The Netherlands, where his research interests included opto-electronic integration, polarization issues, photonic membranes, and photonic crystals. He is the author and coauthor of about 300 publications in the fields of integrated optics and optical networks and holds 30 patent applications. His research interests include modeling of waveguides, design of electro-optical devices on lithium niobate, and their fabrication.